



Cite this: DOI: 10.1039/d0cy01177k

# Ultradeep hydrodesulfurization of fuel over superior NiMoS phases constructed by a novel Ni(MoS<sub>4</sub>)<sub>2</sub>(C<sub>13</sub>H<sub>30</sub>N)<sub>2</sub> precursor†

Jundong Xu, Chenglong Wen, Shuisen He and Yu Fan \*

This article presents novel decyltrimethylammonium bromide-dispersed Ni–Mo sulfide (DTMA–NiMo) as a precursor for preparing an efficient NiMoS/ $\gamma$ -Al<sub>2</sub>O<sub>3</sub> hydrodesulfurization (HDS) catalyst. The as-synthesized DTMA–NiMo is a sulfide containing both long-chain quaternary ammonium and Ni–Mo–S elements. The proposed method not only significantly improves the dispersion of Mo species but also greatly promotes the incorporation of Ni into MoS<sub>2</sub> slabs, leading to an increase in the number of NiMoS phases. As a result, the DTMA–NiMo-based NiMoS/ $\gamma$ -Al<sub>2</sub>O<sub>3</sub> catalyst exhibits much higher activity for the HDS of 4,6-dimethyldibenzothiophene (4,6-DMDBT) and fluid catalytic cracking (FCC) diesel than NiMoS/ $\gamma$ -Al<sub>2</sub>O<sub>3</sub> catalysts prepared by the co-impregnation and tetrapropylammonium bromide (TPAB)-assisted methods. This novel strategy sheds a light on the facile and low-cost preparation of superior NiMoS phases without sulfidation treatment.

Received 10th June 2020,  
Accepted 27th July 2020

DOI: 10.1039/d0cy01177k

rsc.li/catalysis

## 1. Introduction

Hydrodesulfurization (HDS) is one of the most widely used processes to improve fuel quality in the petroleum refining industry.<sup>1</sup> Currently, Ni(Co)–Mo-based sulfides supported on alumina are still the main catalysts used in diesel HDS.<sup>2</sup> However, with the decline in crude-oil quality, the main sulfur-containing compounds in diesel are those with steric hindrance, such as 4,6-DMDBT, which are refractory to removal; thus, the activity of the catalysts needs to be improved.<sup>3–5</sup> In general, bimetallic catalysts are prepared by impregnating alumina with oxidic precursors such as ammonium heptamolybdate and nickel or cobalt salt solutions (simultaneously or successively), followed by drying, calcination and activation *via* sulfidation.<sup>6</sup> In these processes, nickel or cobalt partially reacts with alumina to form Ni(Co) Al<sub>2</sub>O<sub>4</sub> spinels, which are inactive in the HDS reaction; moreover, Mo species can also partially interact with alumina to form Mo–O–Al bonds, which makes sulfidation of the Mo species difficult and decreases the stacking number of MoS<sub>2</sub> slabs.<sup>7–9</sup> As a consequence, nickel or cobalt could not decorate MoS<sub>2</sub> appropriately to form Ni(Co)MoS phases with a high stacking number, which are known as the highly active HDS phases for refractory sulfur-containing compounds.

To enhance the amount of Ni(Co)MoS phases, various methods have been used to prepare Ni(Co)Mo catalysts, such as chemical vapor deposition (CVD),<sup>10–12</sup> the addition of chelating agents (such as nitrilotriacetic acid (NTA), citric acid and ethylenediaminetetraacetic acid (EDTA)),<sup>13,14</sup> and the use of different Ni(Co)Mo precursors (such as oxidic Ni(Co)Mo-based polyoxometalates and Ni(Co)Mo-based bimetallic sulfides).<sup>15–20</sup> Compared to ammonium heptamolybdate and nickel or cobalt salts, Ni(Co)Mo-based polyoxometalates and Ni(Co)Mo-based bimetallic sulfides contain both Ni(Co) and Mo simultaneously, and the close interaction between Ni(Co) and Mo is beneficial for decorating MoS<sub>2</sub> slabs with Ni(Co).<sup>21,22</sup> Griboval *et al.*<sup>23–25</sup> and Thomas *et al.*<sup>26,27</sup> used Keggin-type polyoxometalates (such as Co<sub>3/2</sub>PMo<sub>12</sub>O<sub>40</sub>, Co<sub>7/2</sub>PMo<sub>12</sub>O<sub>40</sub> and Co<sub>2</sub>SiMo<sub>12</sub>O<sub>40</sub>) and Anderson-type polyoxometalates (such as (NH<sub>4</sub>)<sub>3</sub>(CoMo<sub>6</sub>O<sub>24</sub>H<sub>6</sub>)·7H<sub>2</sub>O and (NH<sub>4</sub>)<sub>6</sub>(Co<sub>2</sub>Mo<sub>10</sub>O<sub>38</sub>H<sub>4</sub>·7H<sub>2</sub>O)), respectively, to prepare CoMo/ $\gamma$ -Al<sub>2</sub>O<sub>3</sub> catalysts, and the as-prepared catalysts possessed higher amounts of CoMoS phases than conventional CoMo/Al<sub>2</sub>O<sub>3</sub> HDS catalysts prepared by impregnation. However, the low stability, the low Co/(Co + Mo) atomic ratio (<0.3) and the difficulty of sulfidation of both types of polyoxometalates limit their application.<sup>17</sup> Taniguchi *et al.*<sup>28</sup> used (Mo<sub>3</sub>Ni<sub>4</sub>Cl(H<sub>2</sub>O)<sub>9</sub>)<sup>3+</sup> to prepare NiMo/zeolite catalysts, and the as-prepared catalysts possessed higher HDS activity than conventional NiMo/Al<sub>2</sub>O<sub>3</sub> HDS catalysts prepared by impregnation, but the low Ni/(Ni + Mo) atomic ratio (<0.3), the poor stability and the complex preparation process of (Mo<sub>3</sub>Ni<sub>4</sub>Cl(H<sub>2</sub>O)<sub>9</sub>)<sup>3+</sup> limit its application for the efficient HDS of refractory 4,6-DMDBT.<sup>29</sup>

State Key Laboratory of Heavy Oil Processing, China University of Petroleum, Beijing, 102249, China. E-mail: fanyu@cup.edu.cn; Tel: +86 10 89734981

† Electronic supplementary information (ESI) available. See DOI: 10.1039/d0cy01177k

Herein, we prepared a novel NiMoS/ $\gamma$ -Al<sub>2</sub>O<sub>3</sub> catalyst with a high Ni/Mo ratio, high amount of NiMoS phases and high dispersion of NiMoS phases using decyltrimethylammonium bromide-dispersed Ni–Mo sulfide. In this method, the Ni and Mo species were incorporated into the same sulfide with a high Ni/Mo ratio, which is beneficial for Ni decorating on MoS<sub>2</sub> slabs to form additional NiMoS phases. The as-prepared NiMoS/ $\gamma$ -Al<sub>2</sub>O<sub>3</sub> catalyst exhibited higher activity for HDS of 4,6-DMDBT and FCC diesel compared to NiMoS/ $\gamma$ -Al<sub>2</sub>O<sub>3</sub> catalysts prepared by co-impregnation and tetrapropylammonium bromide (TPAB)-assisted methods.

## 2. Experimental

### 2.1. Materials

The  $\gamma$ -Al<sub>2</sub>O<sub>3</sub> support contained 98.2 wt% Al<sub>2</sub>O<sub>3</sub>, with a pore volume of 0.97 mL g<sup>-1</sup>, surface area of 322 m<sup>2</sup> g<sup>-1</sup> and average diameter of 12.0 nm. 4,6-DMDBT (C<sub>14</sub>H<sub>12</sub>S, 99%) was obtained from Beijing J & K Scientific Ltd (P. R. China). Formamide (CHONH<sub>2</sub>, 99%), TPAB ((CH<sub>3</sub>CH<sub>2</sub>CH<sub>2</sub>)<sub>4</sub>NBr, 99%), decyltrimethylammonium bromide (DTMAB, C<sub>10</sub>H<sub>21</sub>N(CH<sub>3</sub>)<sub>3</sub>Br, 99%) and ammonium tetrathiomolybdate ((NH<sub>4</sub>)<sub>2</sub>MoS<sub>4</sub>, 99%, denoted as ATTM) were obtained from Shanghai Aladdin Biochemical Polytron Technologies Company, Ltd. (P. R. China). Nickel nitrate hexahydrate (Ni(NO<sub>3</sub>)<sub>2</sub>·6H<sub>2</sub>O, 99%), ethanol (C<sub>2</sub>H<sub>5</sub>OH, 99%), naphthane (C<sub>10</sub>H<sub>18</sub>, 99%), *n*-heptane (C<sub>7</sub>H<sub>16</sub>, 99%), cyclohexane (C<sub>6</sub>H<sub>12</sub>, 99%) and carbon disulfide (CS<sub>2</sub>, 99%) were purchased from Beijing Chemical Reagent Company (P. R. China). The above reagents were used directly after purchase without purification.

### 2.2. Synthesis of the sulfided NiMo precursor and preparation of the catalysts

The sulfided NiMo-based precursor was synthesized as follows: first, 0.64 g of (NH<sub>4</sub>)<sub>2</sub>MoS<sub>4</sub> was dissolved in 15 mL of formamide at 10 °C, and 0.36 g of Ni(NO<sub>3</sub>)<sub>2</sub>·6H<sub>2</sub>O was dissolved in 35 mL of deionized water at 10 °C. Then, the nickel nitrate aqueous solution was added slowly to the ATTM solution at 10 °C. Then, 0.89 g of DTMAB was added to the above mixed solution and stirred for 72 h at 10 °C under a N<sub>2</sub> atmosphere, and a resultant black suspension was obtained. Finally, the suspension was suction filtered, washed with ethanol, and dried at 120 °C for 12 h. The acquired product was decyltrimethylammonium-linked NiMo sulfide (denoted as DTMA-NiMo).

A NiMoS/ $\gamma$ -Al<sub>2</sub>O<sub>3</sub> catalyst, designated s-NiMo/ $\gamma$ -Al<sub>2</sub>O<sub>3</sub>-D, was prepared using DTMA-NiMo as a precursor. The typical procedure for preparing s-NiMo/ $\gamma$ -Al<sub>2</sub>O<sub>3</sub>-D was as follows: 1.60 g of the  $\gamma$ -Al<sub>2</sub>O<sub>3</sub> powder was added into a 150 mL round flask containing 50 mL of DTMA-NiMo suspension and stirred for 48 h at 10 °C under a N<sub>2</sub> atmosphere. The obtained product was suction filtered and washed with ethanol. Then, the product was dried under a N<sub>2</sub> atmosphere at 100 °C for 12 h, and the DTMA-NiMo/ $\gamma$ -Al<sub>2</sub>O<sub>3</sub> composite was obtained. Finally, the DTMA-NiMo/ $\gamma$ -Al<sub>2</sub>O<sub>3</sub> composite was calcined at 450 °C for 4 h in a N<sub>2</sub> atmosphere, and s-NiMo/ $\gamma$ -

Al<sub>2</sub>O<sub>3</sub>-D was obtained. The levels of Ni and Mo loaded in s-NiMo/ $\gamma$ -Al<sub>2</sub>O<sub>3</sub>-D were 3.3 and 10.5 wt%, respectively, as detected using an X-ray fluorescence (XRF) spectrometer on an X'Pert Axios apparatus.

For comparison, the other two NiMoS/ $\gamma$ -Al<sub>2</sub>O<sub>3</sub> catalysts were prepared, designated s-NiMo/ $\gamma$ -Al<sub>2</sub>O<sub>3</sub>-T and s-NiMo/ $\gamma$ -Al<sub>2</sub>O<sub>3</sub>-CI. The difference between s-NiMo/ $\gamma$ -Al<sub>2</sub>O<sub>3</sub>-T and s-NiMo/ $\gamma$ -Al<sub>2</sub>O<sub>3</sub>-D was that DTMAB was replaced by TPAB during the preparation process, and the as-prepared precursor was denoted as TPA-NiMo. The s-NiMo/ $\gamma$ -Al<sub>2</sub>O<sub>3</sub>-CI catalyst was prepared by co-impregnation of  $\gamma$ -Al<sub>2</sub>O<sub>3</sub> with an ethanolamine-deionized water solution of ATTM and nickel nitrate. After co-impregnation, the sample was dried in a vacuum oven at 80 °C for 24 h and calcined at 450 °C for 4 h in a N<sub>2</sub> atmosphere. The collected product was s-Mo/ $\gamma$ -Al<sub>2</sub>O<sub>3</sub>-CI. The Ni loads of the s-NiMo/ $\gamma$ -Al<sub>2</sub>O<sub>3</sub>-T and s-NiMo/ $\gamma$ -Al<sub>2</sub>O<sub>3</sub>-CI catalysts detected by XRF were 3.2 and 3.5 wt%, respectively; the Mo loads of the s-NiMo/ $\gamma$ -Al<sub>2</sub>O<sub>3</sub>-T and s-NiMo/ $\gamma$ -Al<sub>2</sub>O<sub>3</sub>-D catalysts were 10.6 and 10.8 wt%, respectively.

### 2.3. Characterization

Elemental analysis of the precursor was performed through inductively coupled plasma-optical emission spectrometry (ICP-OES) on a Perkin-Elmer DV 4300 combined with a 2400 II CHN elemental analyzer. Elemental analyses of the sulfided catalysts were performed on an X'Pert Axios XRF spectrometer.

Raman experiments were performed on a Bruker Raman spectrometer, and the spectra were recorded in 600–100 cm<sup>-1</sup>, using a Nd:YAG laser excited at 532 nm as the laser source.

Fourier transform infrared (FT-IR) analyses were performed on a Bruker 80v (Germany) FT-IR spectrometer with a resolution of 4 cm<sup>-1</sup>. The recorded wavenumber range of the samples was 400–4000 cm<sup>-1</sup>.

X-ray diffraction (XRD) characterization was performed on a PANalytical Advance powder instrument that used Cu K $\alpha$  radiation ( $\lambda = 1.54 \text{ \AA}$ ) and was operated at 40 kV and 40 mA. The scanning speed was 5° min<sup>-1</sup>, and the diffraction lines of 2 $\theta$  were between 10 and 80°.

The pore structure properties of the samples were analyzed by N<sub>2</sub> adsorption–desorption characterization and these experiments were performed on a Micromeritics ASAP 2420 apparatus. Before the experiments, the samples were degassed at 200 °C for 8 h. Then, the samples were subjected to adsorption–desorption at –196 °C.

Transmission electron microscopy (TEM) images of the samples were acquired on an FEI Tecnai G2 F20 instrument equipped with an energy dispersive X-ray spectrometer (EDX). The accelerating voltage was 200 kV, and the point-to-point resolution was 1.9 Å. Before the experiments, the catalysts were kept under a N<sub>2</sub> atmosphere to avoid oxidation. The sample powder was first suspended in ethanol and then dropped onto a carbon polymer-coated copper grid and dried under an infrared lamp.

The sulfided catalysts were analyzed by X-ray photoelectron spectroscopy (XPS). The spectra were acquired on a PHI Quantera SXMTM spectrometer equipped with Al K $\alpha$  radiation operating at 40 eV pass energy. Before the experiments, the catalysts were kept under a N<sub>2</sub> atmosphere to avoid oxidation and then mounted on a holder using double-sided adhesive tape and transferred into the spectrophotometer immediately. The binding energies of the determined elements were corrected by using C1s (284.6 eV) as a reference. The spectra were decomposed by using XPSPEAK version 4.1 software with the mixed Gaussian-Lorentzian function to determine the amounts of Mo<sup>4+</sup>, Mo<sup>5+</sup> and Mo<sup>6+</sup> species and different kinds of Ni species.<sup>30</sup>

The absolute quantification of species *i* ( $C(i)$ ), the effective Ni content in the NiMoS phase ( $C_{\text{NiMoS}}$ ), the effective Mo content in the MoS<sub>2</sub> phase ( $C_{\text{MoS}_2}$ ), and the promoter ratio in the slab edge of the active phase ( $(\text{Ni}/\text{Mo})_{\text{edge}}$ ) were calculated as follows:<sup>31</sup>

$$C(i) = \frac{A_i/S_i}{\sum_{i=1}^n A_i/S_i} \times 100 \quad (1)$$

$$C_{\text{NiMoS}} = \frac{A_{\text{NiMoS}}}{A_{\text{NiMoS}} + A_{\text{NiS}_x} + A_{\text{NiO}_x}} \times C(i) \quad (2)$$

$$C_{\text{MoS}_2} = \frac{A_{\text{MoS}_2}}{A_{\text{MoS}_2} + A_{\text{MoO}_x\text{S}_y} + A_{\text{MoO}_3}} \times C(\text{Mo}) \quad (3)$$

$$(\text{Ni}/\text{Mo})_{\text{edge}} = \frac{C_{\text{NiMoS}}/C_{\text{MoS}_2}}{f_{\text{Mo}}} \quad (4)$$

where  $A_i$  is the calculated area of species *i* and  $S_i$  is the sensitivity factor of atom *i*.

The H<sub>2</sub> temperature-programmed reduction (H<sub>2</sub>-TPR) measurements of the sulfided catalysts were performed on an Auto Chem II 2920 instrument. First, 100 mg of each catalyst was pretreated at 400 °C for 1 h under an Ar atmosphere and cooled to 100 °C. Subsequently, the catalyst was heated from 100 to 800 °C under a 10% H<sub>2</sub>/N<sub>2</sub> flow at a rate of 10 °C min<sup>-1</sup>. H<sub>2</sub> consumption was determined using a TCD detector.

#### 2.4. Catalyst assessment

The HDS performance of s-NiMo/ $\gamma$ -Al<sub>2</sub>O<sub>3</sub>-Cl, s-NiMo/ $\gamma$ -Al<sub>2</sub>O<sub>3</sub>-T and s-NiMo/ $\gamma$ -Al<sub>2</sub>O<sub>3</sub>-D was assessed in a fixed-bed microreactor. The catalyst was loaded into the microreactor after it was sieved through a 20–40 mesh and mixed with quartz granules of the same size and volume. The HDS performance of the catalyst was estimated at a pressure of 4.0 MPa, a H<sub>2</sub>/oil volumetric ratio of 400, a temperature of 320 °C and a liquid hourly space velocity (LHSV) of 20 h<sup>-1</sup> with a feedstock of naphthane solution containing 0.8 wt% 4,6-DMDBT. The product was detected using a Finnigan trace GC-MS. In addition, the HDS performance of the NiMo/ $\gamma$ -Al<sub>2</sub>O<sub>3</sub> catalysts was assessed using FCC diesel. The properties

of FCC diesel are presented in Table S1.† The total sulfur content of FCC diesel was measured using an Analytik Jena Multi EA 5000 (Germany) instrument *via* the pyrolysis method, in accordance with the international standard (ASTM D5453).

The rate constant of HDS ( $k_{\text{HDS}}$ , mol g<sup>-1</sup> s<sup>-1</sup>) was calculated by the following equation:<sup>32</sup>

$$k_{\text{HDS}} = \frac{F}{m} \ln\left(\frac{1}{1-x}\right) \quad (5)$$

where  $F$  is the 4,6-DMDBT rate (mol s<sup>-1</sup>),  $m$  is the catalyst mass (g), and  $x$  is the 4,6-DMDBT conversion. The average stacking number ( $N$ ) and slab length ( $L$ ) were expressed by the following equations.<sup>33</sup>

$$N = \sum x_i N_i / \sum x_i \quad \text{and} \quad L = \sum x_i L_i / \sum x_i \quad (6)$$

where  $N_i$  and  $L_i$  are the layer number and length of MoS<sub>2</sub> slabs in each stack, respectively, and  $x_i$  is the number of MoS<sub>2</sub> slabs with  $N_i$  layers of length  $L_i$ .

The Mo dispersion degree ( $f_{\text{Mo}}$ ) and the turnover frequency (TOF) were calculated according to eqn (7) and (8).<sup>33</sup>

$$f_{\text{Mo}} = \frac{\sum_{i=1}^t (6n_i - 6)}{\sum_{i=1}^t (3n_i^2 - 3n_i + 1)} \quad (7)$$

$$\text{TOF} = \frac{F \times x}{n_{\text{Mo}} \times f_{\text{Mo}}} \quad (8)$$

where  $t$  is the number of total slabs,  $n_i$  is the number of Mo atoms along one edge of a MoS<sub>2</sub> slab,  $x$  is the conversion rate of 4,6-DMDBT,  $F$  is the rate of 4,6-DMDBT turnover (mol s<sup>-1</sup>) and  $n_{\text{Mo}}$  is the amount of Mo atoms in the catalyst (mol).

## 3. Results and discussion

### 3.1. Properties of DTMA-NiMo and determination of DTMA-NiMo loading onto $\gamma$ -Al<sub>2</sub>O<sub>3</sub>

To investigate the properties of DTMA-NiMo, elemental analysis and Raman and FT-IR characterization were performed. The elemental compositions of DTMA-NiMo determined by ICP-OES combined with CHN analysis were

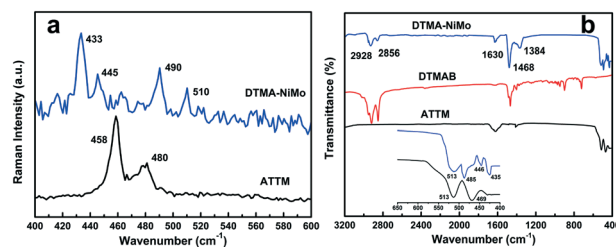


Fig. 1 Raman spectra of ATTM and DTMA-NiMo (a); FT-IR spectra of DTMA-NiMo, ATTM and DTMA-NiMo, the inset shows the 650–400 cm<sup>-1</sup> range for ATTM and DTMA-NiMo (b).

Ni: 6.10 wt%, Mo: 21.22 wt%, C: 35.04 wt%, H: 6.40 wt%, N: 3.08 wt%, and S: 28.16 wt%. Therefore, the DTMA-NiMo composition was  $C_{2.87}H_{6.35}N_{0.22}Ni_{0.11}Mo_{0.22}S_{0.88}$ , almost the same as  $Ni(MoS_4)_2(C_{13}H_{30}N)_2$ . To determine the inorganic core of DTMA-NiMo, the Raman spectra of ATTM and DTMA-NiMo are shown in Fig. 1a. ATTM shows two bands at 458 and 480  $cm^{-1}$ , which are ascribed to the symmetric and asymmetric Mo-S vibrations of  $MoS_4^{2-}$ , respectively.<sup>34</sup> DTMA-NiMo displays the vibrational bands at 433, 445, 490 and 510  $cm^{-1}$ , in which the bands at 433 and 445  $cm^{-1}$  belong to bridging Mo-S stretches and the bands at 490 and 510  $cm^{-1}$  belong to the symmetric and asymmetric Mo-S vibration bands, respectively.<sup>35,36</sup> The symmetric and asymmetric stretching vibration bands of the Mo-S bond in DTMA-NiMo migrates to a higher frequency than those in ATTM, indicating that  $MoS_4^{2-}$  is coordinated with the central metal atom Ni to form  $Ni(MoS_4)_2^{2-}$  in DTMA-NiMo.<sup>35,36</sup> The above analyses demonstrate that the inorganic core of DTMA-NiMo is  $Ni(MoS_4)_2^{2-}$ . Thus,  $Ni(MoS_4)_2^{2-}$  anions interact with DTMA<sup>+</sup> cations to form a DTMA-NiMo compound. To further determine the structure of DTMA-NiMo, FT-IR characterization of DTMA, ATTM and DTMA-NiMo was carried out, and the results are shown in Fig. 1b. In DTMA, the peaks at 2856 and 2928  $cm^{-1}$  are assigned to the stretching vibrations of  $-(CH_2)_n-$  ( $n > 4$ ) and  $-CH_2-$ ,<sup>37</sup> respectively, the peak at 1630  $cm^{-1}$  is attributed to the asymmetric bending vibration of  $(CH_3)_3N^+(NR_4^+)$  in DTMA, and the peak at 1468  $cm^{-1}$  belongs to the shear vibration of  $-CH_2-$ .<sup>38</sup> In the FT-IR spectrum of DTMA-NiMo, there are also characteristic peaks of DTMA in DTMA-NiMo, and the characteristic peak attributed to the  $-CH_3$  bending vibration appears at 1384  $cm^{-1}$ , indicating that DTMA<sup>+</sup> is contained in DTMA-NiMo. In the range of 400–600  $cm^{-1}$ , DTMA-NiMo has vibration peaks at 513, 485, 446 and 435  $cm^{-1}$ . According to the literature,<sup>35,39–41</sup> the peaks at 513 and 485  $cm^{-1}$  belong to the symmetric and asymmetric stretching vibrations of the Mo=S bond, respectively, and the peaks at 446 and 435  $cm^{-1}$  are attributed to bridging Mo-S stretches. The asymmetric stretching vibration peak of the Mo=S bond in DTMA-NiMo migrates to a higher frequency than that in ATTM (the inset of Fig. 1b). This is because the vibration of the Mo=S bond when  $MoS_4^{2-}$  is coordinated with the central metal atom Ni is stronger than that of the Mo=S bond in the uncoordinated  $MoS_4^{2-}$ , which shows that  $Ni(MoS_4)_2^{2-}$  is formed by the interaction of Ni and  $MoS_4^{2-}$  in DTMA-NiMo.<sup>35,42</sup> In addition, in the DTMA-NiMo FT-IR spectrum, except for the peaks attributed to DTMA<sup>+</sup> and  $Ni(MoS_4)_2^{2-}$ , no other peaks appeared. The above analysis shows that DTMA-NiMo is a composite of  $Ni(MoS_4)_2^{2-}$  and DTMA<sup>+</sup>, without other impurities.

To detect the deposition of DTMA-NiMo on  $\gamma-Al_2O_3$ , an  $N_2$  adsorption-desorption experiment was performed. The  $N_2$  adsorption-desorption isotherms and BJH pore size distribution diagrams of  $\gamma-Al_2O_3$ , DTMA-NiMo/ $\gamma-Al_2O_3$  and s-NiMo/ $\gamma-Al_2O_3$ -D are shown in Fig. 2. As seen from Fig. 2a, the  $N_2$  adsorption-desorption isotherms of  $\gamma-Al_2O_3$ , DTMA-NiMo/

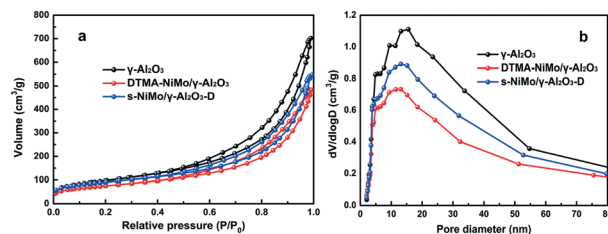


Fig. 2  $N_2$  adsorption-desorption isotherms (a) and BJH pore size distribution curves (b) of  $\gamma-Al_2O_3$ , DTMA-NiMo/ $\gamma-Al_2O_3$  and s-NiMo/ $\gamma-Al_2O_3$ -D.

$\gamma-Al_2O_3$  and s-NiMo/ $\gamma-Al_2O_3$ -D are type IV, indicating that they have the characteristics of mesoporous materials; the hysteresis ring is type H3, suggesting the presence of slit-type pores.<sup>43</sup> Fig. 2b shows that the introduction of DTMA-NiMo into  $\gamma-Al_2O_3$  reduces the size of the latter most probable pore size. The results in Table 1 show that the average pore diameter, pore volume and specific surface area of DTMA-NiMo/ $\gamma-Al_2O_3$  are smaller than those of  $\gamma-Al_2O_3$ , suggesting the loading of DTMA-NiMo onto  $\gamma-Al_2O_3$ . The specific surface area, pore volume and average pore diameter of s-NiMo/ $\gamma-Al_2O_3$ -D with calcination at 450  $^\circ C$  are higher than those of DTMA-NiMo/ $\gamma-Al_2O_3$  without calcination due to the decomposition of the organic carbon chains in DTMA-NiMo, which proves that DTMA-NiMo is loaded onto  $\gamma-Al_2O_3$ . To further prove the loading of DTMA-NiMo onto  $\gamma-Al_2O_3$ , an s-NiMo/ $\gamma-Al_2O_3$ -DE catalyst was prepared using alumina extrudates as a support. s-NiMo/ $\gamma-Al_2O_3$ -DE has almost the same TEM results (Fig. S1†) and the same 4,6-DMDBT HDS activity (Table S2†) as s-NiMo/ $\gamma-Al_2O_3$ -D. These results prove the successful deposition of DTMA-NiMo into the support pores.

### 3.2. Characterization of the sulfided NiMoS/ $\gamma-Al_2O_3$ catalysts

**3.2.1. XRD and  $N_2$  adsorption-desorption.** To explore the dispersion of active metals on  $\gamma-Al_2O_3$ , the as-prepared NiMoS/ $\gamma-Al_2O_3$  catalysts were characterized by XRD, and the results are shown in Fig. 3. All the catalysts presented characteristic peaks at  $2\theta = 37.4^\circ$ ,  $45.7^\circ$  and  $67^\circ$  (JCPDS card no. 29-1486), which are attributed to  $\gamma-Al_2O_3$ . In addition, s-NiMo/ $\gamma-Al_2O_3$ -CI and s-NiMo/ $\gamma-Al_2O_3$ -T also have peaks at  $2\theta = 33.5^\circ$  and  $58.3^\circ$  (JCPDS card no. 37-1492) belonging to the  $MoS_2$  (101) and (110) planes. However, there is no

Table 1 Textural properties of  $\gamma-Al_2O_3$ , s-NiMo/ $\gamma-Al_2O_3$ -CI, s-NiMo/ $\gamma-Al_2O_3$ -T and s-NiMo/ $\gamma-Al_2O_3$ -D

Sample	$S_{BET}^a$ ( $m^2 g^{-1}$ )	$V_p^b$ ( $cm^3 g^{-1}$ )	$D_p^c$ (nm)
$\gamma-Al_2O_3$	322	0.97	12.0
DTMA-NiMo/ $\gamma-Al_2O_3$	224	0.52	9.3
s-NiMo/ $\gamma-Al_2O_3$ -CI	258	0.64	9.9
s-NiMo/ $\gamma-Al_2O_3$ -T	263	0.66	10.0
s-NiMo/ $\gamma-Al_2O_3$ -D	297	0.82	11.0

<sup>a</sup> BET specific surface area. <sup>b</sup> Pore volume. <sup>c</sup> Average pore diameter ( $4 V_p/S_g$ ).

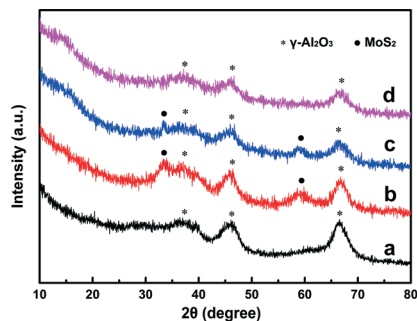


Fig. 3 XRD patterns of  $\gamma$ -Al<sub>2</sub>O<sub>3</sub> (a), s-NiMo/ $\gamma$ -Al<sub>2</sub>O<sub>3</sub>-Cl (b), s-NiMo/ $\gamma$ -Al<sub>2</sub>O<sub>3</sub>-T (c) and s-NiMo/ $\gamma$ -Al<sub>2</sub>O<sub>3</sub>-D (d).

characteristic peak attributed to MoS<sub>2</sub> in s-NiMo/ $\gamma$ -Al<sub>2</sub>O<sub>3</sub>-D, indicating that compared with s-NiMo/ $\gamma$ -Al<sub>2</sub>O<sub>3</sub>-Cl and s-NiMo/ $\gamma$ -Al<sub>2</sub>O<sub>3</sub>-T, s-NiMo/ $\gamma$ -Al<sub>2</sub>O<sub>3</sub>-D presents a smaller particle size of Mo species on the surface of  $\gamma$ -Al<sub>2</sub>O<sub>3</sub>. Because of the low loading of nickel in the NiMoS/ $\gamma$ -Al<sub>2</sub>O<sub>3</sub> catalysts, no characteristic peak of nickel species appears in the XRD pattern of NiMoS/ $\gamma$ -Al<sub>2</sub>O<sub>3</sub>.

The pore structure parameters of  $\gamma$ -Al<sub>2</sub>O<sub>3</sub>, s-NiMo/ $\gamma$ -Al<sub>2</sub>O<sub>3</sub>-Cl, s-NiMo/ $\gamma$ -Al<sub>2</sub>O<sub>3</sub>-T and s-NiMo/ $\gamma$ -Al<sub>2</sub>O<sub>3</sub>-D are listed in Table 1. Compared with the  $\gamma$ -Al<sub>2</sub>O<sub>3</sub> support, the specific surface areas of s-NiMo/ $\gamma$ -Al<sub>2</sub>O<sub>3</sub>-Cl, s-NiMo/ $\gamma$ -Al<sub>2</sub>O<sub>3</sub>-T and s-NiMo/ $\gamma$ -Al<sub>2</sub>O<sub>3</sub>-D are reduced by 19.9%, 18.3% and 7.8%, respectively; the pore volumes are reduced by 34.0%, 32.0%, and 15.5%, respectively; and the average pore diameters are decreased by 17.5%, 16.7%, and 8.3%, respectively. These decreases are attributed to the deposition of active metals. s-NiMo/ $\gamma$ -Al<sub>2</sub>O<sub>3</sub>-Cl and s-NiMo/ $\gamma$ -Al<sub>2</sub>O<sub>3</sub>-T have similar average pore diameters, pore volumes and specific surface areas; however, compared with s-NiMo/ $\gamma$ -Al<sub>2</sub>O<sub>3</sub>-Cl and s-NiMo/ $\gamma$ -Al<sub>2</sub>O<sub>3</sub>-T, s-NiMo/ $\gamma$ -Al<sub>2</sub>O<sub>3</sub>-D has a larger average pore diameter, pore volume and specific surface area. According to the above XRD characterization results, the particle size of Mo species on s-NiMo/ $\gamma$ -Al<sub>2</sub>O<sub>3</sub>-D is smaller than those on s-NiMo/ $\gamma$ -Al<sub>2</sub>O<sub>3</sub>-Cl and s-NiMo/ $\gamma$ -Al<sub>2</sub>O<sub>3</sub>-T, so it has minimal influence on the pore structure of the  $\gamma$ -Al<sub>2</sub>O<sub>3</sub> support. The above analysis

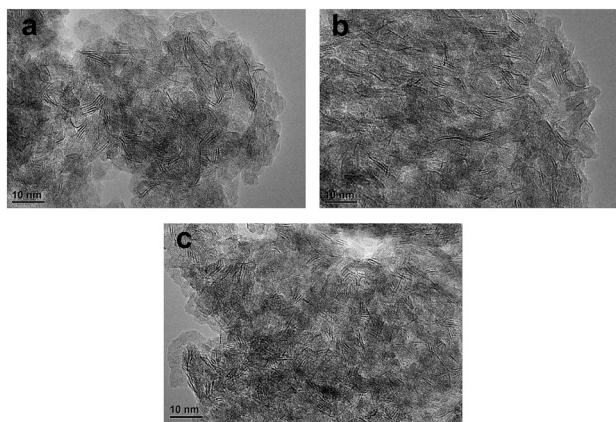


Fig. 4 HRTEM images of s-NiMo/ $\gamma$ -Al<sub>2</sub>O<sub>3</sub>-Cl (a), s-NiMo/ $\gamma$ -Al<sub>2</sub>O<sub>3</sub>-T (b) and s-NiMo/ $\gamma$ -Al<sub>2</sub>O<sub>3</sub>-D (c).

shows that s-NiMo/ $\gamma$ -Al<sub>2</sub>O<sub>3</sub>-D has the best pore structure among the three catalysts, which is beneficial for promoting the diffusion of 4,6-DMDBT in the catalyst and thereby improving the HDS activity of s-NiMo/ $\gamma$ -Al<sub>2</sub>O<sub>3</sub>-D.

**3.2.2. HRTEM.** The typical HRTEM images of s-NiMo/ $\gamma$ -Al<sub>2</sub>O<sub>3</sub>-Cl, s-NiMo/ $\gamma$ -Al<sub>2</sub>O<sub>3</sub>-T and s-NiMo/ $\gamma$ -Al<sub>2</sub>O<sub>3</sub>-D are shown in Fig. 4. According to the EDX analysis results, the black thread-like fringes in the images are MoS<sub>2</sub> slabs. The interlayer distance between the black thread-like fringes is 0.62 nm, which is consistent with the distance between the (002) characteristic plane of the MoS<sub>2</sub> crystal.<sup>44</sup> Most of the MoS<sub>2</sub> slabs on s-NiMo/ $\gamma$ -Al<sub>2</sub>O<sub>3</sub>-Cl and s-NiMo/ $\gamma$ -Al<sub>2</sub>O<sub>3</sub>-T are long while most of the MoS<sub>2</sub> slabs on s-NiMo/ $\gamma$ -Al<sub>2</sub>O<sub>3</sub>-D are short, indicating that s-NiMo/ $\gamma$ -Al<sub>2</sub>O<sub>3</sub>-D has superior active-metal dispersion.

To further understand the lengths and stacking numbers of the supported active metals, statistical analyses were conducted on the basis of approximately 20 images, containing 400–600 black thread-like fringes obtained from different regions of each catalyst, and the statistical results are shown in Fig. 5. The lengths of MoS<sub>2</sub> slabs in s-NiMo/ $\gamma$ -Al<sub>2</sub>O<sub>3</sub>-Cl and s-NiMo/ $\gamma$ -Al<sub>2</sub>O<sub>3</sub>-T are mainly concentrated at 3.0–5.0 nm, while those in s-NiMo/ $\gamma$ -Al<sub>2</sub>O<sub>3</sub>-D are mainly concentrated at 2.0–4.0 nm. For s-NiMo/ $\gamma$ -Al<sub>2</sub>O<sub>3</sub>-Cl and s-NiMo/ $\gamma$ -Al<sub>2</sub>O<sub>3</sub>-T, the percentages of MoS<sub>2</sub> slabs with lengths longer than 4.0 nm are 44.7% and 55.2%, respectively; for s-NiMo/ $\gamma$ -Al<sub>2</sub>O<sub>3</sub>-D, only 19.5% of MoS<sub>2</sub> slabs has lengths longer than 4.0 nm, indicating that the use of DTMA-NiMo as a precursor significantly decreases the lengths of MoS<sub>2</sub> slabs. From Fig. 5b, the distributions of the stacking numbers of MoS<sub>2</sub> slabs in s-NiMo/ $\gamma$ -Al<sub>2</sub>O<sub>3</sub>-Cl, s-NiMo/ $\gamma$ -Al<sub>2</sub>O<sub>3</sub>-T and s-NiMo/ $\gamma$ -Al<sub>2</sub>O<sub>3</sub>-D are all concentrated in 3–4 layers, indicating that the three catalysts have almost identical stacking numbers of MoS<sub>2</sub> slabs.

According to eqn (6), the average stacking numbers and the average lengths of MoS<sub>2</sub> slabs in s-NiMo/ $\gamma$ -Al<sub>2</sub>O<sub>3</sub>-Cl, s-NiMo/ $\gamma$ -Al<sub>2</sub>O<sub>3</sub>-T and s-NiMo/ $\gamma$ -Al<sub>2</sub>O<sub>3</sub>-D were calculated as shown in Table 2. Combined with eqn (7), the dispersion degree ( $f_{\text{Mo}}$ ) of MoS<sub>2</sub> slabs in the three bimetallic catalysts was calculated as shown in Table 2. The dispersion degree, the average stacking number and the average length of MoS<sub>2</sub> slabs in s-NiMo/ $\gamma$ -Al<sub>2</sub>O<sub>3</sub>-Cl are 0.25, 3.3 layers and 4.2 nm, respectively. The average stacking number of MoS<sub>2</sub> slabs in s-NiMo/ $\gamma$ -Al<sub>2</sub>O<sub>3</sub>-T is almost the same as that of s-NiMo/ $\gamma$ -Al<sub>2</sub>O<sub>3</sub>-

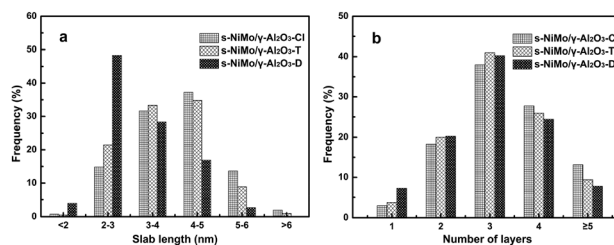


Fig. 5 Statistical distributions of the lengths (a) and stacking numbers (b) of MoS<sub>2</sub> slabs on s-NiMo/ $\gamma$ -Al<sub>2</sub>O<sub>3</sub>-Cl, s-NiMo/ $\gamma$ -Al<sub>2</sub>O<sub>3</sub>-T and s-NiMo/ $\gamma$ -Al<sub>2</sub>O<sub>3</sub>-D.

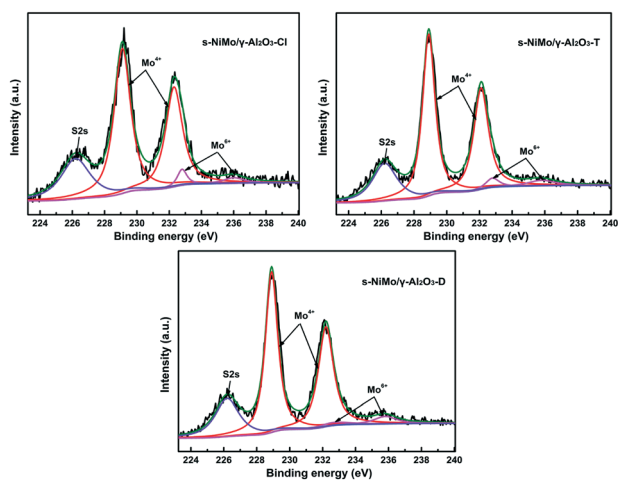
**Table 2** HRTEM statistical results for s-NiMo/ $\gamma$ -Al<sub>2</sub>O<sub>3</sub>-Cl, s-NiMo/ $\gamma$ -Al<sub>2</sub>O<sub>3</sub>-T and s-NiMo/ $\gamma$ -Al<sub>2</sub>O<sub>3</sub>-D

Catalyst	<i>L</i> (nm)	<i>N</i>	<i>f</i> <sub>Mo</sub>
s-NiMo/ $\gamma$ -Al <sub>2</sub> O <sub>3</sub> -Cl	4.2	3.3	0.25
s-NiMo/ $\gamma$ -Al <sub>2</sub> O <sub>3</sub> -T	4.0	3.2	0.27
s-NiMo/ $\gamma$ -Al <sub>2</sub> O <sub>3</sub> -D	2.9	3.1	0.36

Cl; however, the average length of MoS<sub>2</sub> slabs in s-NiMo/ $\gamma$ -Al<sub>2</sub>O<sub>3</sub>-T is slightly shorter than that in s-NiMo/ $\gamma$ -Al<sub>2</sub>O<sub>3</sub>-Cl, and the dispersion degree of MoS<sub>2</sub> slabs in s-NiMo/ $\gamma$ -Al<sub>2</sub>O<sub>3</sub>-T is slightly higher than that in s-NiMo/ $\gamma$ -Al<sub>2</sub>O<sub>3</sub>-Cl. The average stacking number of MoS<sub>2</sub> slabs in s-NiMo/ $\gamma$ -Al<sub>2</sub>O<sub>3</sub>-D is almost the same as that in s-NiMo/ $\gamma$ -Al<sub>2</sub>O<sub>3</sub>-Cl, but the average length of MoS<sub>2</sub> slabs in s-NiMo/ $\gamma$ -Al<sub>2</sub>O<sub>3</sub>-D is much lower than that in s-NiMo/ $\gamma$ -Al<sub>2</sub>O<sub>3</sub>-Cl, and the dispersion degree of MoS<sub>2</sub> slabs in s-NiMo/ $\gamma$ -Al<sub>2</sub>O<sub>3</sub>-D is much higher than that in s-NiMo/ $\gamma$ -Al<sub>2</sub>O<sub>3</sub>-Cl. These results indicate that the catalyst prepared with DTMA-NiMo as a precursor has good Mo dispersion.

**3.2.3. XPS.** To further understand the chemical state, dispersion degree, sulfurization degree and surface composition of the active metals in the prepared catalysts, XPS characterization of s-NiMo/ $\gamma$ -Al<sub>2</sub>O<sub>3</sub>-Cl, s-NiMo/ $\gamma$ -Al<sub>2</sub>O<sub>3</sub>-T and s-NiMo/ $\gamma$ -Al<sub>2</sub>O<sub>3</sub>-D was performed. According to the literature,<sup>45,46</sup> the background of the Mo3d secondary electron spectrum was subtracted, and then the peak decomposition was performed (Shirley method). The ratio of the half width of 3d<sub>3/2</sub> to the half width of 3d<sub>5/2</sub> is approximately 1.2, and the relative area of 3d<sub>3/2</sub> to the relative area of 3d<sub>5/2</sub> is approximately 1.5.

The experimental and fitting results of the Mo3d XPS spectra of s-NiMo/ $\gamma$ -Al<sub>2</sub>O<sub>3</sub>-Cl, s-NiMo/ $\gamma$ -Al<sub>2</sub>O<sub>3</sub>-T and s-NiMo/ $\gamma$ -Al<sub>2</sub>O<sub>3</sub>-D are shown in Fig. 6. The Mo3d<sub>5/2</sub> and Mo3d<sub>3/2</sub> binding energies in the MoS<sub>2</sub> (Mo<sup>4+</sup>) phase are 229.0 ± 0.1 eV and 232.1 ± 0.1 eV, respectively; the Mo3d<sub>5/2</sub> and Mo3d<sub>3/2</sub> binding energies in the intermediate MoO<sub>x</sub>S<sub>y</sub> (Mo<sup>5+</sup>) phase are 230.2 ± 0.1 eV and 233.4 ± 0.1 eV, respectively; the Mo3d<sub>5/2</sub>

**Fig. 6** Mo 3d XPS patterns of s-NiMo/ $\gamma$ -Al<sub>2</sub>O<sub>3</sub>-Cl, s-NiMo/ $\gamma$ -Al<sub>2</sub>O<sub>3</sub>-T and s-NiMo/ $\gamma$ -Al<sub>2</sub>O<sub>3</sub>-D.

and Mo3d<sub>3/2</sub> binding energies in the MoO<sub>3</sub> (Mo<sup>6+</sup>) phase are 232.2 ± 0.1 eV and 235.3 ± 0.1 eV, respectively.<sup>30</sup> The binding energy at 226.0 ± 0.1 eV is ascribed to S2s.<sup>47</sup> In s-NiMo/ $\gamma$ -Al<sub>2</sub>O<sub>3</sub>-Cl, s-NiMo/ $\gamma$ -Al<sub>2</sub>O<sub>3</sub>-T and s-NiMo/ $\gamma$ -Al<sub>2</sub>O<sub>3</sub>-D, there are no peaks belonging to the oxidation state MoO<sub>x</sub>S<sub>y</sub> (Mo<sup>5+</sup>) phase.

This is because the above three catalysts were all prepared by using a sulfur-containing molybdenum compound as a precursor, which is directly decomposed into MoS<sub>2</sub> during calcination without going through the oxidic MoO<sub>x</sub>S<sub>y</sub> intermediates. The Mo sulfidation degree (Mo<sub>sulfidation</sub>) is defined as Mo<sub>sulfidation</sub> = Mo<sup>4+</sup>/(Mo<sup>4+</sup> + Mo<sup>5+</sup> + Mo<sup>6+</sup>),<sup>32,48</sup> and Mo<sup>4+</sup>, Mo<sup>5+</sup> and Mo<sup>6+</sup> represent the levels of the MoS<sub>2</sub> (Mo<sup>4+</sup>), MoO<sub>x</sub>S<sub>y</sub> (Mo<sup>5+</sup>) and MoO<sub>3</sub> (Mo<sup>6+</sup>) phases, respectively. The XPS fitting results in Table 3 show that the Mo sulfidation degrees of s-NiMo/ $\gamma$ -Al<sub>2</sub>O<sub>3</sub>-Cl, s-NiMo/ $\gamma$ -Al<sub>2</sub>O<sub>3</sub>-T and s-NiMo/ $\gamma$ -Al<sub>2</sub>O<sub>3</sub>-D are 93.2%, 93.5% and 93.6%, indicating almost full sulfidation of Mo species in the three catalysts. The much higher sulfidation degrees of s-NiMo/ $\gamma$ -Al<sub>2</sub>O<sub>3</sub>-Cl, s-NiMo/ $\gamma$ -Al<sub>2</sub>O<sub>3</sub>-T and s-NiMo/ $\gamma$ -Al<sub>2</sub>O<sub>3</sub>-D compared to that of commercial NiMo/Al<sub>2</sub>O<sub>3</sub> result from the use of ammonium tetrathiomolybdate ((NH<sub>4</sub>)<sub>2</sub>MoS<sub>4</sub>) as the molybdenum precursor rather than ammonium heptamolybdate.<sup>49</sup>

The experimental and fitting results of the Ni2p spectra for s-NiMo/ $\gamma$ -Al<sub>2</sub>O<sub>3</sub>-Cl, s-NiMo/ $\gamma$ -Al<sub>2</sub>O<sub>3</sub>-T and s-NiMo/ $\gamma$ -Al<sub>2</sub>O<sub>3</sub>-D are shown in Fig. 7. In general, on the sulfided NiMo bimetallic catalysts, nickel species exist in the form of NiO<sub>x</sub>, NiS<sub>x</sub> (Ni<sub>2</sub>S<sub>3</sub>, Ni<sub>9</sub>S<sub>8</sub> and NiS) and NiMoS phases. According to the literature,<sup>30,50,51</sup> the peaks of Ni2p spectra were decomposed. The Ni 2p spectra contain NiO<sub>x</sub> peaks at 855.8, 858.4, and 861.7 eV, NiS<sub>x</sub> peaks at 852.9 and 855.0 eV, and NiMoS peaks at 853.3 and 856.0 eV, and the relative levels of the NiO<sub>x</sub>, NiS<sub>x</sub> and NiMoS phases calculated are listed in Table 3. The percentage of the NiMoS phase in s-NiMo/ $\gamma$ -Al<sub>2</sub>O<sub>3</sub>-D is 79.1%, which is higher than those in s-NiMo/ $\gamma$ -Al<sub>2</sub>O<sub>3</sub>-Cl (52.7%) and s-NiMo/ $\gamma$ -Al<sub>2</sub>O<sub>3</sub>-T (67.2%). The higher percentage of the NiMoS phase in s-NiMo/ $\gamma$ -Al<sub>2</sub>O<sub>3</sub>-D results from the promoting effect of its high MoS<sub>2</sub> dispersion on the generation of NiMoS phases because the MoS<sub>2</sub> slabs can serve as a secondary support for nickel species.<sup>52,53</sup>

In Table 3, the (Ni/Mo)<sub>edge</sub> ratio of s-NiMo/ $\gamma$ -Al<sub>2</sub>O<sub>3</sub>-D (1.22) is higher than those of s-NiMo/ $\gamma$ -Al<sub>2</sub>O<sub>3</sub>-Cl (0.81) and s-NiMo/ $\gamma$ -Al<sub>2</sub>O<sub>3</sub>-T (0.98), which indicates that the decoration degree of Ni on the edges of MoS<sub>2</sub> in s-NiMo/ $\gamma$ -Al<sub>2</sub>O<sub>3</sub>-D is better than those in s-NiMo/ $\gamma$ -Al<sub>2</sub>O<sub>3</sub>-Cl and s-NiMo/ $\gamma$ -Al<sub>2</sub>O<sub>3</sub>-T.<sup>47</sup> The much higher relative content of Ni in NiMoS and the higher (Ni/Mo)<sub>edge</sub> ratio over s-NiMo/ $\gamma$ -Al<sub>2</sub>O<sub>3</sub>-D than those over s-NiMo/ $\gamma$ -Al<sub>2</sub>O<sub>3</sub>-Cl and s-NiMo/ $\gamma$ -Al<sub>2</sub>O<sub>3</sub>-T indicate that, compared with the co-impregnation and tetrapropylammonium bromide (TPAB)-assisted methods, the novel precursor method facilitates Ni decoration on MoS<sub>2</sub> slabs to form a high number of NiMoS phases.

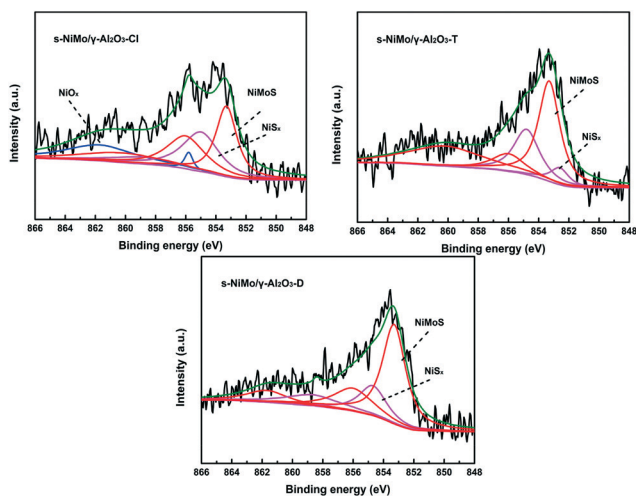
The surface atomic ratios of Mo/Al and Ni/Al in s-NiMo/ $\gamma$ -Al<sub>2</sub>O<sub>3</sub>-Cl, s-NiMo/ $\gamma$ -Al<sub>2</sub>O<sub>3</sub>-T and s-NiMo/ $\gamma$ -Al<sub>2</sub>O<sub>3</sub>-D were detected by XPS, and the results are shown in Table 3. Though the three catalysts possess almost the same metal contents, s-NiMo/ $\gamma$ -Al<sub>2</sub>O<sub>3</sub>-D has a higher surface atomic ratio

**Table 3** Fitting results of XPS on s-NiMo/ $\gamma$ -Al<sub>2</sub>O<sub>3</sub>-Cl, s-NiMo/ $\gamma$ -Al<sub>2</sub>O<sub>3</sub>-T and s-NiMo/ $\gamma$ -Al<sub>2</sub>O<sub>3</sub>-D

Catalyst	Mo/Al	Ni/Al	Mo <sub>Sulfidation</sub> (%)	Ni fraction (%)			(Ni/Mo) <sub>edge</sub>
				NiO <sub>x</sub>	NiS <sub>x</sub>	NiMoS	
s-NiMo/ $\gamma$ -Al <sub>2</sub> O <sub>3</sub> -Cl	0.092	0.032	93.2	18.4	28.9	52.7	0.81
s-NiMo/ $\gamma$ -Al <sub>2</sub> O <sub>3</sub> -T	0.121	0.037	93.5	—	32.8	67.2	0.98
s-NiMo/ $\gamma$ -Al <sub>2</sub> O <sub>3</sub> -D	0.142	0.042	93.6	—	20.9	79.1	1.22

than the other two catalysts, indicating the better dispersion of NiMoS phases supported on s-NiMo/ $\gamma$ -Al<sub>2</sub>O<sub>3</sub>-D as compared to s-NiMo/ $\gamma$ -Al<sub>2</sub>O<sub>3</sub>-Cl and s-NiMo/ $\gamma$ -Al<sub>2</sub>O<sub>3</sub>-T.<sup>54</sup>

**3.2.4. H<sub>2</sub>-TPR.** The H<sub>2</sub>-TPR characterization of the sulfided s-NiMo/ $\gamma$ -Al<sub>2</sub>O<sub>3</sub>-Cl, s-NiMo/ $\gamma$ -Al<sub>2</sub>O<sub>3</sub>-T and s-NiMo/ $\gamma$ -Al<sub>2</sub>O<sub>3</sub>-D catalysts provides the information about the strength of the Mo-S bond and the relative number of surface active sites.<sup>55,56</sup> Fig. 8 shows the H<sub>2</sub>-TPR patterns of s-NiMo/ $\gamma$ -Al<sub>2</sub>O<sub>3</sub>-Cl, s-NiMo/ $\gamma$ -Al<sub>2</sub>O<sub>3</sub>-T and s-NiMo/ $\gamma$ -Al<sub>2</sub>O<sub>3</sub>-D. The three catalysts have similar characteristic peaks, corresponding to the high-intensity resolution peak in the low-temperature region (210 °C) and the low-intensity broad peak in the high-temperature region. According to the literature,<sup>56–58</sup> the reduction peak in the low-temperature region is ascribed to the reduction of sulfur atoms at the edge of MoS<sub>2</sub> with weak Mo-S bonding strength. The low-temperature reduction peak temperatures of s-NiMo/ $\gamma$ -Al<sub>2</sub>O<sub>3</sub>-Cl, s-NiMo/ $\gamma$ -Al<sub>2</sub>O<sub>3</sub>-T and s-NiMo/ $\gamma$ -Al<sub>2</sub>O<sub>3</sub>-D are 223, 219 and 213 °C, respectively. The temperature of the low-temperature reduction peak on s-NiMo/ $\gamma$ -Al<sub>2</sub>O<sub>3</sub>-D is lower than those on s-NiMo/ $\gamma$ -Al<sub>2</sub>O<sub>3</sub>-Cl and s-NiMo/ $\gamma$ -Al<sub>2</sub>O<sub>3</sub>-T because the former has a higher dispersion of Mo sulfides as demonstrated by the above HRTEM characterization. These results indicate that s-NiMo/ $\gamma$ -Al<sub>2</sub>O<sub>3</sub>-D has a higher reducibility than s-NiMo/ $\gamma$ -Al<sub>2</sub>O<sub>3</sub>-Cl and s-NiMo/ $\gamma$ -Al<sub>2</sub>O<sub>3</sub>-T.<sup>56</sup> In addition, s-NiMo/ $\gamma$ -Al<sub>2</sub>O<sub>3</sub>-D has a much higher low-temperature peak area than s-NiMo/ $\gamma$ -Al<sub>2</sub>O<sub>3</sub>-Cl and s-NiMo/ $\gamma$ -Al<sub>2</sub>O<sub>3</sub>-T because the former has more NiMoS phases as demonstrated by the above XPS characterization.

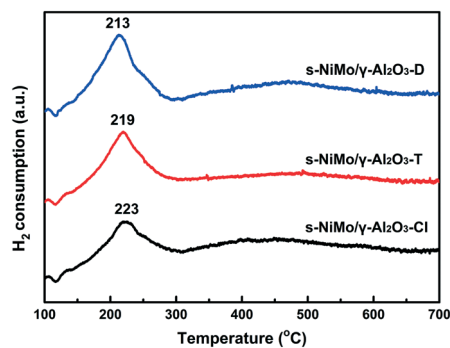
**Fig. 7** Ni 2p XPS spectra of s-NiMo/ $\gamma$ -Al<sub>2</sub>O<sub>3</sub>-Cl, s-NiMo/ $\gamma$ -Al<sub>2</sub>O<sub>3</sub>-T and s-NiMo/ $\gamma$ -Al<sub>2</sub>O<sub>3</sub>-D.

### 3.3. Catalytic activity

A naphthane solution containing 0.8 wt% 4,6-DMDBT was used as a feedstock to evaluate the HDS activity of s-NiMo/ $\gamma$ -Al<sub>2</sub>O<sub>3</sub>-Cl, s-NiMo/ $\gamma$ -Al<sub>2</sub>O<sub>3</sub>-T and s-NiMo/ $\gamma$ -Al<sub>2</sub>O<sub>3</sub>-D. The HDS reaction rate constants ( $k_{\text{HDS}}$ ) and TOF values of s-NiMo/ $\gamma$ -Al<sub>2</sub>O<sub>3</sub>-Cl, s-NiMo/ $\gamma$ -Al<sub>2</sub>O<sub>3</sub>-T and s-NiMo/ $\gamma$ -Al<sub>2</sub>O<sub>3</sub>-D at 4 MPa, a H<sub>2</sub>/oil volumetric ratio of 400 and 320 °C are listed in Table 4. The  $k_{\text{HDS}}$  value of s-NiMo/ $\gamma$ -Al<sub>2</sub>O<sub>3</sub>-D is  $6.35 \times 10^{-7}$  mol g<sup>-1</sup> s<sup>-1</sup>, which is 2.05 times that of s-NiMo/ $\gamma$ -Al<sub>2</sub>O<sub>3</sub>-Cl and 1.69 times that of s-NiMo/ $\gamma$ -Al<sub>2</sub>O<sub>3</sub>-T. The TOF value of s-NiMo/ $\gamma$ -Al<sub>2</sub>O<sub>3</sub>-D is  $10.01 \times 10^{-4}$  s<sup>-1</sup>, which is 1.66 times that of s-NiMo/ $\gamma$ -Al<sub>2</sub>O<sub>3</sub>-Cl and 1.40 times that of s-NiMo/ $\gamma$ -Al<sub>2</sub>O<sub>3</sub>-T. The TOF and  $k_{\text{HDS}}$  values of s-NiMo/ $\gamma$ -Al<sub>2</sub>O<sub>3</sub>-D are higher than those of s-NiMo/ $\gamma$ -Al<sub>2</sub>O<sub>3</sub>-Cl and s-NiMo/ $\gamma$ -Al<sub>2</sub>O<sub>3</sub>-T, indicating that s-NiMo/ $\gamma$ -Al<sub>2</sub>O<sub>3</sub>-D has better HDS activity than s-NiMo/ $\gamma$ -Al<sub>2</sub>O<sub>3</sub>-Cl and s-NiMo/ $\gamma$ -Al<sub>2</sub>O<sub>3</sub>-T.

The reaction pathways of 4,6-DMDBT on NiMoS/ $\gamma$ -Al<sub>2</sub>O<sub>3</sub> are shown in Fig. 9.<sup>59</sup> The HDS of 4,6-DMDBT on NiMoS/ $\gamma$ -Al<sub>2</sub>O<sub>3</sub> mainly includes the following pathways: hydrogenation reaction (HYD) and direct desulfurization reaction (DDS). The primary products detected during 4,6-DMDBT HDS on NiMoS/ $\gamma$ -Al<sub>2</sub>O<sub>3</sub> are: 3,3'-dimethylbicyclohexane (3,3'-DMBCH), 4,6-hexahydrodimethyldibenzothiophene (4,6-HHDMDBT), 3,3'-dimethylbiphenyl (3,3'-DMBP), 3,3'-dimethylcyclohexyltoluene (3,3'-MCHT) and 4,6-tetrahydrodimethyldibenzothiophene (4,6-THDMDBT).<sup>3,60</sup>

At the identical conversion (50%) of 4,6-DMDBT, the HDS product distributions of the three bimetallic catalysts were compared, and the results are listed in Table 4. The molar ratios of 3,3'-MCHT to 3,3'-DMBP in the reaction products of 4,6-DMDBT HDS on all catalysts are higher than 1, which shows that the HDS of 4,6-DMDBT on s-NiMo/ $\gamma$ -Al<sub>2</sub>O<sub>3</sub>-Cl, s-

**Fig. 8** H<sub>2</sub>-TPR patterns of s-NiMo/ $\gamma$ -Al<sub>2</sub>O<sub>3</sub>-Cl, s-NiMo/ $\gamma$ -Al<sub>2</sub>O<sub>3</sub>-T and s-NiMo/ $\gamma$ -Al<sub>2</sub>O<sub>3</sub>-D.

**Table 4** HDS results for 4,6-DMDBT on s-NiMo/ $\gamma$ -Al<sub>2</sub>O<sub>3</sub>-Cl, s-NiMo/ $\gamma$ -Al<sub>2</sub>O<sub>3</sub>-T and s-NiMo/ $\gamma$ -Al<sub>2</sub>O<sub>3</sub>-D

Catalyst	$K_{\text{HDS}}^a$ (10 <sup>-7</sup> mol g <sup>-1</sup> s <sup>-1</sup> )	TOF <sup>a</sup> × 10 <sup>4</sup> (s <sup>-1</sup> )	Product selectivity (%)				Product ratio	
			TH + HH	MCHT	DMBCH	DMBP	(TH + HH)/MCHT	MCHT/DMBP
s-NiMo/ $\gamma$ -Al <sub>2</sub> O <sub>3</sub> -Cl	3.10	6.03	10.3	54.7	4.0	31.0	0.19	1.76
s-NiMo/ $\gamma$ -Al <sub>2</sub> O <sub>3</sub> -T	3.76	7.14	7.5	59.4	4.9	28.2	0.13	2.11
s-NiMo/ $\gamma$ -Al <sub>2</sub> O <sub>3</sub> -D	6.35	10.01	5.3	63.7	5.5	24.5	0.08	2.60

<sup>a</sup> Calculated with the 4,6-DMDBT conversion at about 10%.

NiMo/ $\gamma$ -Al<sub>2</sub>O<sub>3</sub>-T and s-NiMo/ $\gamma$ -Al<sub>2</sub>O<sub>3</sub>-D is mainly carried out by the HYD route. This is mainly due to the steric hindrance effect of 4,6-DMDBT at its positions 4 and 6, which inhibits the interaction between the sulfur atoms and the active metal centers, making it difficult for 4,6-DMDBT to generate  $\sigma$  adsorption with the active metal centers through the vertical adsorption of sulfur atoms.<sup>61</sup> However, the methyl groups at the 4 and 6 positions will not affect 4,6-DMDBT to generate  $\sigma$  adsorption with the active metal centers through the horizontal adsorption of the aromatic ring.<sup>62</sup> Therefore, the desulfurization reaction *via* the HYD pathway is dominant during 4,6-DMDBT HDS.<sup>63</sup> The molar ratio of 3,3'-MCHT to 3,3'-DMBP in the HDS product of 4,6-DMDBT on s-NiMo/ $\gamma$ -Al<sub>2</sub>O<sub>3</sub>-D is higher than those on s-NiMo/ $\gamma$ -Al<sub>2</sub>O<sub>3</sub>-Cl and s-NiMo/ $\gamma$ -Al<sub>2</sub>O<sub>3</sub>-T, which shows that s-NiMo/ $\gamma$ -Al<sub>2</sub>O<sub>3</sub>-D has a better HYD activity than s-NiMo/ $\gamma$ -Al<sub>2</sub>O<sub>3</sub>-Cl and s-NiMo/ $\gamma$ -Al<sub>2</sub>O<sub>3</sub>-T.

Conventional NiMo/ $\gamma$ -Al<sub>2</sub>O<sub>3</sub> (3.8 wt% Ni and 11.0 wt% Mo, designated NiMo/ $\gamma$ -Al<sub>2</sub>O<sub>3</sub>-C) prepared by impregnating alumina with the solutions of ammonium heptamolybdate and nickel nitrate was also selected as a reference catalyst to evaluate the activities and stabilities of the as-prepared catalysts. The time course of changes in total sulfur levels in the 4,6-DMDBT model oil HDS product with reaction on NiMo/ $\gamma$ -Al<sub>2</sub>O<sub>3</sub>-C, s-NiMo/ $\gamma$ -Al<sub>2</sub>O<sub>3</sub>-Cl, s-NiMo/ $\gamma$ -Al<sub>2</sub>O<sub>3</sub>-T and s-NiMo/ $\gamma$ -Al<sub>2</sub>O<sub>3</sub>-D is shown in Fig. 10. Under the reaction conditions of 320 °C, 4.0 MPa, a LHSV of 20 h<sup>-1</sup>, and a H<sub>2</sub>/oil volumetric ratio 400, NiMo/ $\gamma$ -Al<sub>2</sub>O<sub>3</sub>-C, s-NiMo/ $\gamma$ -Al<sub>2</sub>O<sub>3</sub>-Cl, s-NiMo/ $\gamma$ -Al<sub>2</sub>O<sub>3</sub>-T and s-NiMo/ $\gamma$ -Al<sub>2</sub>O<sub>3</sub>-D exhibit stable sulfur levels in the HDS products of 4,6-DMDBT model oil within 142 h of operation time. This proves that the four catalysts have good HDS stability. In addition, the HDS activities of the four catalysts using FCC diesel as a feedstock were

further investigated. The total sulfur content in the feed was 3640  $\mu\text{g g}^{-1}$ , and the reaction conditions were 350 °C, 6.0 MPa, a LHSV of 2.5 h<sup>-1</sup>, and a H<sub>2</sub>/oil volumetric ratio 400. From Table 5, s-NiMo/ $\gamma$ -Al<sub>2</sub>O<sub>3</sub>-D has the highest HDS ratio among the four catalysts, indicating its superiority in the HDS of FCC diesel. These results indicate that s-NiMo/ $\gamma$ -Al<sub>2</sub>O<sub>3</sub>-D has application potential in the ultra-deep HDS of FCC diesel.

### 3.4. Origin of the active phase structures of the catalysts

The above characterization results indicate that s-NiMo/ $\gamma$ -Al<sub>2</sub>O<sub>3</sub>-D prepared with DTMA-NiMo as a precursor has high Mo dispersion and a great number of NiMoS phases. To explore the influence of TPA-NiMo and DTMA-NiMo as precursors on the morphology of Mo species in the prepared s-NiMo/ $\gamma$ -Al<sub>2</sub>O<sub>3</sub>-T and s-NiMo/ $\gamma$ -Al<sub>2</sub>O<sub>3</sub>-D, the TPA-NiMo and DTMA-NiMo precursor suspensions were characterized by TEM, as shown in Fig. 11. The statistical analysis result for the nanoparticle size on DTMA-NiMo, obtained by measuring at least 500 nanoparticles, is shown in the inset of Fig. 11a. The nanoparticle size of DTMA-NiMo is mainly distributed at 2.4–3.2 nm. The DTMA-NiMo composites are highly dispersed and uniform nanoparticles with an average particle size of approximately 3.0 nm (Fig. 11a and b). Unlike the uniformly monodispersed nanoparticles of DTMA-NiMo, TPA-NiMo mainly exists in the form of large aggregates (Fig. 11c and d). The different existing states of DTMA-NiMo and TPA-NiMo are explained as follows: in DTMA-NiMo, each DTMA-NiMo nanoparticle has two long carbon chains, and the long carbon chains have strong hydrophobic-hydrophilic

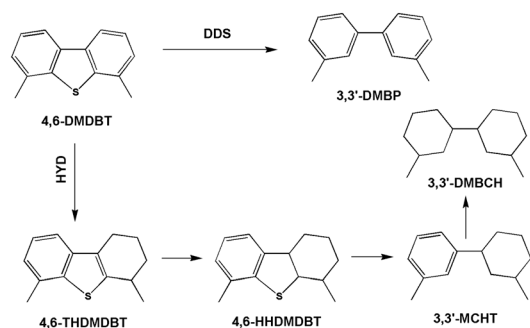


**Fig. 9** Reaction network of 4,6-DMDBT HDS on these catalysts.

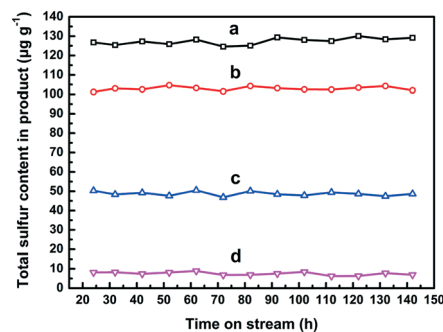


**Fig. 10** Total sulfur levels in the product of 4,6-DMDBT HDS over the reaction time on NiMo/ $\gamma$ -Al<sub>2</sub>O<sub>3</sub>-C (a), s-NiMo/ $\gamma$ -Al<sub>2</sub>O<sub>3</sub>-Cl (b), s-NiMo/ $\gamma$ -Al<sub>2</sub>O<sub>3</sub>-T (c) and s-NiMo/ $\gamma$ -Al<sub>2</sub>O<sub>3</sub>-D (d).

**Table 5** FCC diesel HDS results for s-NiMo/ $\gamma$ -Al<sub>2</sub>O<sub>3</sub>-Cl, s-NiMo/ $\gamma$ -Al<sub>2</sub>O<sub>3</sub>-T and s-NiMo/ $\gamma$ -Al<sub>2</sub>O<sub>3</sub>-D

Catalyst	Total sulfur content in feedstock ( $\mu\text{g g}^{-1}$ )	Total sulfur content in feedstock ( $\mu\text{g g}^{-1}$ )	HDS ratio (%)
NiMo/ $\gamma$ -Al <sub>2</sub> O <sub>3</sub> -C	3640	208.7	94.3
s-NiMo/ $\gamma$ -Al <sub>2</sub> O <sub>3</sub> -Cl	3640	194.5	94.7
s-NiMo/ $\gamma$ -Al <sub>2</sub> O <sub>3</sub> -T	3640	132.3	96.4
s-NiMo/ $\gamma$ -Al <sub>2</sub> O <sub>3</sub> -D	3640	7.2	99.8

repulsion with the surrounding water molecules.<sup>64</sup> This effect makes DTMA-NiMo uniformly monodispersed in the synthetic solution. However, the TPA-NiMo particles have short carbon chains, which lead to weak hydrophobic-hydrophilic repulsion with the surrounding water molecules.<sup>65,66</sup> As a consequence, the particles of TPA-NiMo are suspended in the synthetic solution in the form of large aggregates.

According to the above analyses, the preparation principles for s-NiMo/ $\gamma$ -Al<sub>2</sub>O<sub>3</sub>-D and s-NiMo/ $\gamma$ -Al<sub>2</sub>O<sub>3</sub>-T are proposed in Fig. 12. During the deposition process, the long alkyl carbon chains around the nanoparticles of DTMA-NiMo can inhibit the aggregation of NiMo species and DTMA-NiMo is uniformly monodispersed in the synthetic solution with fine nanoparticles; after adding  $\gamma$ -Al<sub>2</sub>O<sub>3</sub>, these nanoparticles can be effectively deposited on the surface of  $\gamma$ -Al<sub>2</sub>O<sub>3</sub> with high dispersion. During the drying process, the interaction between the long alkyl carbon chains around DTMA-NiMo nanoparticles leads to an increase in the solution viscosity with vaporization of the solvent, effectively inhibiting the redistribution of the solution and thereby restraining the aggregation of DTMA-NiMo nanoparticles.<sup>7</sup> During calcination in a N<sub>2</sub> atmosphere, the carbonization of the long carbon chains on the outer layer of DTMA-NiMo produces a barrier for the aggregation of NiMo species and further improves the dispersion of NiMo species. For s-NiMo/ $\gamma$ -Al<sub>2</sub>O<sub>3</sub>-T, during the deposition process, because TPA-NiMo exists in the synthetic solution in the form of large aggregates, it is difficult for TPA-NiMo to accumulate on the surface of

$\gamma$ -Al<sub>2</sub>O<sub>3</sub> in the form of monodispersed nanoparticles after the addition of  $\gamma$ -Al<sub>2</sub>O<sub>3</sub>. During the drying process, the alkyl carbon chains around TPA-NiMo are relatively short, resulting in the basically unchanged viscosity of the solution with vaporization of the solvent;<sup>54,64</sup> therefore, the solution is redistributed, and TPA-NiMo is further aggregated. During calcination in a N<sub>2</sub> atmosphere, it is difficult to effectively improve the dispersion of NiMo species due to the aggregation of TPA-NiMo particles during the initial deposition and subsequent drying process, despite the carbonization of the carbon chains present in TPA-NiMo. Therefore, compared with s-NiMo/ $\gamma$ -Al<sub>2</sub>O<sub>3</sub>-T, s-NiMo/ $\gamma$ -Al<sub>2</sub>O<sub>3</sub>-D has a higher dispersion of NiMoS phases.

The HDS evaluation results of 4,6-DMDBT and real FCC diesel have proven that s-NiMo/ $\gamma$ -Al<sub>2</sub>O<sub>3</sub>-D has better HDS activity than s-NiMo/ $\gamma$ -Al<sub>2</sub>O<sub>3</sub>-Cl and s-NiMo/ $\gamma$ -Al<sub>2</sub>O<sub>3</sub>-T. The XRD and N<sub>2</sub> adsorption-desorption characterization results have shown that s-NiMo/ $\gamma$ -Al<sub>2</sub>O<sub>3</sub>-D has smaller metal species than s-NiMo/ $\gamma$ -Al<sub>2</sub>O<sub>3</sub>-Cl and s-NiMo/ $\gamma$ -Al<sub>2</sub>O<sub>3</sub>-T, which improve the accessibility of active phases. As demonstrated by the XPS results, s-NiMo/ $\gamma$ -Al<sub>2</sub>O<sub>3</sub>-D has more NiMoS phases than s-NiMo/ $\gamma$ -Al<sub>2</sub>O<sub>3</sub>-Cl and s-NiMo/ $\gamma$ -Al<sub>2</sub>O<sub>3</sub>-T, which enhance the efficiency of 4,6-DMDBT HDS. The HRTEM results have proved that s-NiMo/ $\gamma$ -Al<sub>2</sub>O<sub>3</sub>-D, s-NiMo/ $\gamma$ -Al<sub>2</sub>O<sub>3</sub>-Cl and s-NiMo/ $\gamma$ -Al<sub>2</sub>O<sub>3</sub>-T have MoS<sub>2</sub> slabs with about 3-layer stackings, guaranteeing good accessibility of NiMoS active phases for 4,6-DMDBT. s-NiMo/ $\gamma$ -Al<sub>2</sub>O<sub>3</sub>-Cl and s-NiMo/ $\gamma$ -Al<sub>2</sub>O<sub>3</sub>-T with low dispersion degrees of 0.25 and 0.27, respectively, have relatively few exposed NiMoS phases, which weakens their 4,6-DMDBT HDS performance. In contrast, s-NiMo/ $\gamma$ -Al<sub>2</sub>O<sub>3</sub>-D, with a high dispersion degree of 0.36 has a sufficient number of exposed NiMoS phases, which enhances both the HYD and DDS routes for 4,6-DMDBT HDS. Therefore, s-NiMo/ $\gamma$ -Al<sub>2</sub>O<sub>3</sub>-D, with sufficient and accessible NiMoS active phases, allows

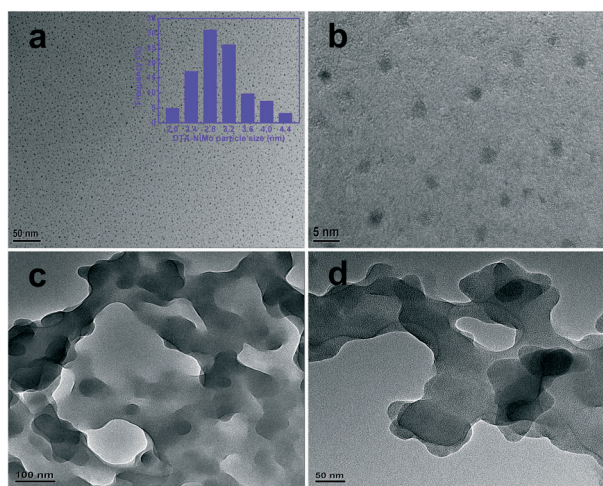


**Fig. 11** TEM images of DTMA-NiMo (a and b), size distribution of DTMA-NiMo (the inset of a) and TEM images of TPA-NiMo (c and d).

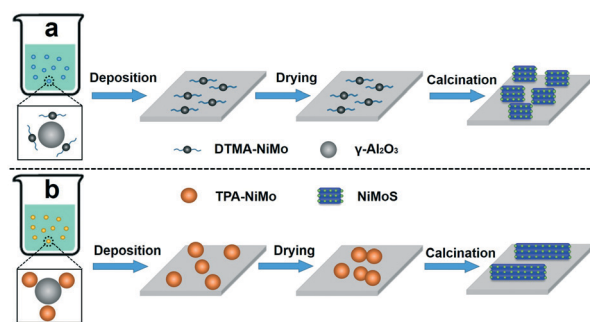


**Fig. 12** Schematic diagram of the preparation principles of s-NiMo/ $\gamma$ -Al<sub>2</sub>O<sub>3</sub>-D (a) and s-NiMo/ $\gamma$ -Al<sub>2</sub>O<sub>3</sub>-T (b).

efficient adsorption and HDS reactions of refractory sulfur-containing compounds with steric hindrance.

## 4. Conclusions

Novel decyltrimethylammonium bromide-dispersed Ni–Mo sulfide (DTMA–NiMo) was adopted for preparing a highly efficient NiMoS/ $\gamma$ -Al<sub>2</sub>O<sub>3</sub> HDS catalyst. The Ni and Mo species were incorporated into the same sulfide with a high Ni/Mo ratio, which is beneficial for improving the decoration of MoS<sub>2</sub> slabs by Ni to form a high number of NiMoS phases. The as-synthesized NiMoS phases on the  $\gamma$ -Al<sub>2</sub>O<sub>3</sub> support have superior active-metal morphology, with a high dispersion of 0.36 and suitable stacking numbers (approximately 3.0), offering a large number of accessible NiMoS phases. The as-prepared NiMoS/ $\gamma$ -Al<sub>2</sub>O<sub>3</sub> catalyst exhibits much higher activity for the HDS of 4,6-DMDBT and FCC diesel than NiMoS/ $\gamma$ -Al<sub>2</sub>O<sub>3</sub> catalysts prepared by co-impregnation and TPAB-assisted methods. This method provides a novel and facile route for the production of sufficient and accessible NiMoS phases in HDS catalysts for ultra-deep HDS of fuel.

## Conflicts of interest

There are no conflicts to declare.

## Acknowledgements

The authors gratefully acknowledge the financial support of the National Natural Science Foundation of China (Grant No. 21978323).

## References

- 1 A. Tanimu and K. Alhooshani, *Energy Fuels*, 2019, **33**, 2810–2838.
- 2 A. Stanislaus, A. Marafi and M. S. Rana, *Catal. Today*, 2010, **153**, 1–68.
- 3 S. K. Bej, S. K. Maity and U. T. Turaga, *Energy Fuels*, 2004, **18**, 1227–1237.
- 4 Q. Zhang, J. Zhang, H. Yang, Y. Dong, Y. Liu, L. Yang, D. Wei, W. Wang, L. Bai and H. Chen, *Catal. Sci. Technol.*, 2019, **9**, 2915–2922.
- 5 M. Zuo, X. Huang, J. Li, Q. Chang, Y. Duan, L. Yan, Z. Xiao, S. Mei, S. Lu and Y. Yao, *Catal. Sci. Technol.*, 2019, **9**, 2923–2930.
- 6 M. Breyse, C. Geantet, P. Afanasiev, J. Blanchard and M. Vrinat, *Catal. Today*, 2008, **130**, 3–13.
- 7 A. J. van Dillen, R. J. A. M. Terörde, D. J. Lensveld, J. W. Geus and K. P. de Jong, *J. Catal.*, 2003, **216**, 257–264.
- 8 J. A. Bergwerff, T. Visser, G. Leliveld, B. D. Rossenaar, K. P. de Jong and B. M. Weckhuysen, *J. Am. Chem. Soc.*, 2004, **126**, 14548–14556.
- 9 J. A. Bergwerff, T. Visser and B. M. Weckhuysen, *Catal. Today*, 2008, **130**, 117–125.
- 10 P. Serp, P. Kalck and R. Feurer, *Chem. Rev.*, 2002, **102**, 3085–3128.
- 11 Z. Liu, M. Amani, S. Najmaei, Q. Xu, X. Zou, W. Zhou, T. Yu, C. Qiu, A. G. Birdwell, F. J. Crowne, R. Vajtai, B. I. Yakobson, Z. Xia, M. Dubey, P. M. Ajayan and J. Lou, *Nat. Commun.*, 2014, **5**, 5246–5254.
- 12 H. U. Rashid, K. Yu, M. N. Umar, M. N. Anjum, K. Khan, N. Ahmad and M. T. Jan, *Rev. Adv. Mater. Sci.*, 2015, **40**, 235–248.
- 13 E. Hensen, P. Kooyman, Y. Van der Meer, A. Van der Kraan, V. De Beer, J. Van Veen and R. Van Santen, *J. Catal.*, 2001, **199**, 224–235.
- 14 M. S. Rana, J. Ramírez, A. Gutiérrez-Alejandre, J. Ancheyta, L. Cedeño and S. Maity, *J. Catal.*, 2007, **246**, 100–108.
- 15 P. A. Nikul'shin, Y. V. Eremina, N. N. Tomina and A. A. Pimerzin, *Pet. Chem.*, 2006, **46**, 343–348.
- 16 N. N. Tomina, P. A. Nikul'shin and A. A. Pimerzin, *Pet. Chem.*, 2008, **48**, 92–99.
- 17 O. V. Klimov, A. V. Pashigreva, G. A. Bukhtiyarova, S. V. Budukva, M. A. Fedotov, D. I. Kochubey, Y. A. Chesalov, V. I. Zaikovskii and A. S. Noskov, *Catal. Today*, 2010, **150**, 196–206.
- 18 J. Liang, M. Wu, P. Wei, J. Zhao, H. Huang, C. Li, Y. Lu, Y. Liu and C. Liu, *J. Catal.*, 2018, **358**, 155–167.
- 19 J. Liang, M. Wu, J. Wang, P. Wei, B. Sun, Y. Lu, D. Sun, Y. Liu and C. Liu, *Catal. Sci. Technol.*, 2018, **8**, 6330–6345.
- 20 M. S. Nikulshina, P. Blanchard, A. Mozhaev, C. Lancelot, A. Griboval-Constant, M. Fournier, E. Payen, O. Mentré, V. Briois, P. A. Nikulshin and C. Lamonier, *Catal. Sci. Technol.*, 2018, **8**, 5557–5572.
- 21 A. J. A. Konings, A. Valster, V. H. J. de Beer and R. Prins, *J. Catal.*, 1982, **76**, 466–472.
- 22 M. Feliz, R. Llusar, S. Uriel, C. Vicent, M. Brorson and K. Herbst, *Polyhedron*, 2005, **24**, 1212–1220.
- 23 A. Griboval, P. Blanchard, E. Payen, M. Fournier and J. L. Dubois, *Catal. Today*, 1998, **45**, 277–283.
- 24 A. Griboval, P. Blanchard, L. Gengembre, E. Payen, M. Fournier, J. L. Dubois and J. R. Bernard, *J. Catal.*, 1999, **188**, 102–110.
- 25 A. Griboval, P. Blanchard, E. Payen, M. Fournier, J. L. Dubois and J. R. Bernard, *Appl. Catal., A*, 2001, **217**, 173–183.
- 26 C. I. Cabello, I. L. Botto and H. J. Thomas, *Appl. Catal., A*, 2000, **197**, 79–86.
- 27 C. I. Cabello, F. M. Cabrerizo, A. Alvarez and H. J. Thomas, *J. Mol. Catal. A: Chem.*, 2002, **186**, 89–100.
- 28 M. Taniguchi, D. Imamura, H. Ishige, Y. Ishii, T. Murata, M. Hidai and T. Tatsumi, *J. Catal.*, 1999, **187**, 139–150.
- 29 K. Herbst, M. Monari and M. Brorson, *Inorg. Chem.*, 2001, **40**, 2979–2985.
- 30 T. K. T. Ninh, L. Massin, D. Laurenti and M. Vrinat, *Appl. Catal., A*, 2011, **407**, 29–39.
- 31 P. A. Nikulshin, D. I. Ishutenko, A. A. Mozhaev, K. I. Maslakov and A. A. Pimerzin, *J. Catal.*, 2014, **312**, 152–169.
- 32 J. Xu, T. Huang and Y. Fan, *Appl. Catal., B*, 2017, **203**, 839–850.
- 33 S. Liu, X. Liang, J. Zhang and B. Chen, *Catal. Sci. Technol.*, 2017, **7**, 466–480.

- 34 T. Weber, J. C. Muijsers and J. W. Niemantsverdriet, *J. Chem. Phys.*, 1995, **99**, 9194–9200.
- 35 A. Müller, E. Diemann, R. Jostes and H. Bögge, *Angew. Chem., Int. Ed. Engl.*, 1981, **20**, 934–955.
- 36 R. J. H. Clark and J. R. Walton, *J. Chem. Soc., Dalton Trans.*, 1987, 1535–1544.
- 37 T. Ito, K. Sawada and T. Yamase, *Chem. Lett.*, 2003, **32**, 938–939.
- 38 G. Huang, T. Chen, W. Chen, Z. Wang, K. Chang, L. Ma, F. Huang, D. Chen and J. Y. Lee, *Small*, 2013, **9**, 3693–3703.
- 39 E. Diemann and A. Müller, *Coord. Chem. Rev.*, 1973, **10**, 79–122.
- 40 E. Koeniger-Ahlborn, A. Mueller, A. D. Cormier, J. D. Brown and K. Nakamoto, *Inorg. Chem.*, 1975, **14**, 2009–2011.
- 41 I. Sötofte, *Acta Chem. Scand., Ser. A*, 1976, **30**, 157–162.
- 42 W.-H. Pan, D. C. Johnston, S. T. McKenna, R. R. Chianelli, T. R. Halbert, L. L. Hutchings and E. I. Stiefel, *Inorg. Chim. Acta*, 1985, **97**, L17–L19.
- 43 C. Liu, J. Li, Y. Zhang, S. Chen, J. Zhu and K. Liew, *J. Mol. Catal. A: Chem.*, 2012, **363-364**, 335–342.
- 44 E. Payen, R. Hubaut, S. Kasztelan, O. Poulet and J. Grimblot, *J. Catal.*, 1994, **147**, 123–132.
- 45 A. M. Venezia, *Catal. Today*, 2003, **77**, 359–370.
- 46 A. D. Gandubert, C. Legens, D. Guillaume and E. Payen, *Surf. Interface Anal.*, 2006, **38**, 206–209.
- 47 P. A. Nikulshin, A. Mozhaev, K. Maslakov, A. Pimerzin and V. Kogan, *Appl. Catal., B*, 2014, **158**, 161–174.
- 48 T. Huang, J. Chang, S. He, C. Wen and Y. Fan, *Energy Fuels*, 2019, **33**, 135–147.
- 49 X. Li, Y. Chai, B. Liu, H. Liu, J. Li, R. Zhao and C. Liu, *Ind. Eng. Chem. Res.*, 2014, **53**, 9665–9673.
- 50 W. Lai, L. Pang, J. Zheng, J. Li, Z. Wu, X. Yi, W. Fang and L. Jia, *Fuel Process. Technol.*, 2013, **110**, 8–16.
- 51 W. Zhou, M. Liu, Q. Zhang, Q. Wei, S. Ding and Y. Zhou, *ACS Catal.*, 2017, **7**, 7665–7679.
- 52 T. Shimizu, K. Hiroshima, T. Honma, T. Mochizuki and M. Yamada, *Catal. Today*, 1998, **45**, 271–276.
- 53 Y. Okamoto, K. Ochiai, M. Kawano and T. Kubota, *J. Catal.*, 2004, **222**, 143–151.
- 54 W. Han, P. Yuan, Y. Fan, G. Shi, H. Liu, D. Bai and X. Bao, *J. Mater. Chem.*, 2012, **22**, 25340–25353.
- 55 C. J. H. Jacobsen, E. Törnqvist and H. Topsøe, *Catal. Lett.*, 1999, **63**, 179–183.
- 56 P. Afanasiev, *Appl. Catal., A*, 2006, **303**, 110–115.
- 57 B. Liu, Y. Chai, Y. Li, A. Wang, Y. Liu and C. Liu, *Appl. Catal., A*, 2014, **471**, 70–79.
- 58 P. Li, X. Liu, C. Zhang, Y. Chen, B. Huang, T. Liu, Z. Jiang and C. Li, *Appl. Catal., A*, 2016, **524**, 66–76.
- 59 K. Sakanishi, T. Nagamatsu, I. Mochida and D. D. Whitehurst, *J. Mol. Catal. A: Chem.*, 2000, **155**, 101–109.
- 60 M. Egorova and R. Prins, *J. Catal.*, 2004, **225**, 417–427.
- 61 H. Wang and R. Prins, *J. Catal.*, 2009, **264**, 31–43.
- 62 X. Wang, Z. Zhao, P. Zheng, Z. Chen, A. Duan, C. Xu, J. Jiao, H. Zhang, Z. Cao and B. Ge, *J. Catal.*, 2016, **344**, 680–691.
- 63 A. Niquille-Röthlisberger and R. Prins, *J. Catal.*, 2006, **242**, 207–216.
- 64 S. Paria and K. C. Khilar, *Adv. Colloid Interface Sci.*, 2004, **110**, 75–95.
- 65 Z. Zhang, M. A. Horsch, M. H. Lamm and S. C. Glotzer, *Nano Lett.*, 2003, **3**, 1341–1346.
- 66 R. B. Grubbs, *Polym. Rev.*, 2007, **47**, 197–215.